Supporting information

Asymmetric two-dimensional nanomembranes for salinity gradient energy conversion

Sungsoon Kim,[a,b] Hong Choi,[a,b] Jihun Yeom,[a,b] Taeyoung Kim,[a,b] Taehoon Kim,[a,b] Ji Hoon Han,[a,b] Jongbum Won,[a,b] Minwoo Lee,[a,b] Hyesoo Kim,[a,b] Jihong Bae,[a,b] Bokyeong Kim, [a,b] Geonwoo Lim,[a,b] Juan Bisquert,[c] Wooyoung Shim[a,b,d,e*]

[a] Department of Materials Science and Engineering, Yonsei University, Seoul 120-749, South Korea

[b] Center for Multi-Dimensional Materials, Yonsei University, Seoul 03722, South Korea

[c] Instituto de Tecnología Química (Universitat Politècnica de València-Consejo Superior de Investigaciones Científicas), València 46022, Spain

[d] Center for Nanomedicine, Institute for Basic Science (IBS), Seoul 03722, South Korea

[e] Yonsei IBS Institute, Yonsei University, Seoul 03722, South Korea

This PDF file includes:

Experimental Methods

Materials and reagents. VMT crystals were purchased from Hansung Industry (Gunsan, South Korea), and NaCl (99%) and LiCl (98%) were purchased from Duksan Science (Ansan, South Korea) and used as received. The Ag/AgCl ink and textile electrodes were purchased from ALS (Tokyo, Japan) and Woiron (Ghangzhou, China), respectively.

Fabrication of the VMT membranes. A stable Li-VMT suspension was used to fabricate the P-VMT membrane, which was synthesized via two-step ion-exchange exfoliation. First, 2 g of Expanded VMT crystals were immersed per 100 mL of a saturated NaCl solution, which was then continuously stirred at 95 °C for 24 h. The obtained precipitate, Na ion-VMT, was then vacuum filtered with repeated washing using deionized (DI) H_2O. The Na ion-VMT was then redispersed in 500 mL of a 2 M LiCl solution with continuous stirring at 95 °C for 24 h. Finally, fully substituted Li ion-VMT was then vacuum filtered and thoroughly washed with DI H_2O. The product was dispersed in DI H_2O and ultrasonicated for 60 min to exfoliate Li-VMT, followed by high-speed centrifugation at 5000 rpm for 60 min. The supernatant was then collected, yielding a stable light brown suspension of monolayer VMT nanosheets. A VMT membrane with an average thickness of 3 μm was prepared by vacuum filtering 5 mL of the suspension onto a polyvinylidene fluoride substrate. The obtained membrane was dried for 24 h under ambient conditions before removal via peeling. The PE-VMT membrane was fabricated by exposing a partially confined VMT membrane to a high temperature of 700 °C. To measure the ionic conductivity and salinity-gradient energy conversion performance, a custom-built cell consisting of two reservoirs was employed. High- and low-salinity solutions were independently loaded into the respective reservoirs, which were designed to be ionically connected exclusively through the membrane-mounting region. The P-VMT and PE–VMT membranes were oriented such that ion transport occurred predominantly along the horizontal (intramembrane) direction. After mounting, the membrane edges and surrounding junction

regions were encapsulated with epoxy to minimize leakage pathways and to ensure mechanical stability of the laminated structure during measurements.

Fabrication of the cell, device, and module. Large-area PE-VMT membranes (cell, device, and module) were fabricated via the vertical stacking and self-healing of PE-VMT films. Before stacking, the surfaces of the PE-VMT films were uniformly moisturized using a commercial humidifier to facilitate self-healing and seamless vertical adhesion between the films. After each five-layer stack, OHP films were attached using epoxy resin (DEVCON S-209, ITW Performance Polymers, Danvers, MA, USA) to reinforce the structural durability. A stack of 30 PE-VMT films was produced and then further encapsulated by adhering additional OHP films on the top and bottom surfaces and sealing the lateral sides with epoxy resin to mitigate the swelling induced by prolonged wet conditions. The excess epoxy resin introduced during fabrication was subsequently removed via the mechanical polishing of the surfaces of the membranes.

The module comprised 30 individual devices arranged in series within a PP reservoir container. Each device was fixed securely at the central partition walls of the container using epoxy resin. Device-to-device electrical connections within the module were realized using the Ag/AgCl ink and textile electrodes. The resistances between the connected devices were carefully controlled at 0.1 Ω, optimizing the overall module performance.

Electrochemical measurements. We used a digital multimeter (34401A, Keysight, Santa Rosa, CA, USA) and picoammeter (Keithley 6487, Tektronix, Beaverton, OR, USA) in the electrical measurements. All measurements were performed at 25 °C.

Characterization. SEM was performed using a JSM-7001F scanning electron microscope (JEOL, Tokyo, Japan). XPS, XRD, and FT-IR spectroscopy were respectively performed using a K-Alpha spectrometer (Thermo Fisher Scientific, Waltham, MA, USA) with

Al Kα (1486.6 eV) radiation as the X-ray source, an Ultima IV X-ray diffractometer (Rigaku, Tokyo, Japan) with Cu Kα (λ = 1.5418 Å) radiation (40 kV, 150 mA), and a Vertex 70 (Bruker, Billerica, MA, USA).

Numerical simulations. Numerical calculations were performed using a simplified 1D model to quantitatively analyze the mechanism of ion transport within the PE-VMT membrane, because the geometrical asymmetry of PE-VMT occurred only in the 1D direction. The respective channel heights of C-VMT and E-VMT were defined as 1 and 6.5 nm, as limited by the program resolution (0.5 nm) and minimum computational dimension. The calculations were based on the Poisson and Nernst–Planck (PNP) equations describing ion migration and diffusion influenced by electric fields and concentration gradients, respectively. The electric field induced by the surface charges on the channel surfaces was calculated using the Poisson–Boltzmann equation. These calculations were implemented in ANSYS Fluent (ANSYS, Canonsburg, PA, USA) via the magnetohydrodynamics model by incorporating the channel surface charges as boundary conditions. The governing equations used are as follows.

Poisson–Boltzmann equation:

$$\nabla^2\varphi = -\frac{F\sum_i z_i c_i}{\epsilon_r}$$

$$\vec{n}\cdot\nabla\varphi = -\frac{\sigma}{\epsilon}$$

Steady-state Nernst–Planck equation:

$$j_i = D_i\left(\nabla c_i + \frac{z_i F c_i}{RT}\nabla\varphi\right),$$

where φ, F, z_i, c_i, ε_r, σ, j_i, D_i, R, and T represent the electrical potential, Faraday's constant, ionic valence, ion concentration, relative permittivity, surface charge, ion flux densities, ion diffusivity, gas constant, and absolute temperature, respectively. For simplification, the diffusivity coefficients of the cations and anions are assumed to be identical.

The boundary conditions specify that no ion flux normal to the boundary occurs:

$$\vec{n} \cdot \vec{j_i} = 0.$$

As ANSYS does not support the required equations and parameters, these were introduced using user-defined functions and scalars.

Note S1. Redox potential of electrodes (V_{redox})

To interpret the measured open-circuit voltage in salinity-gradient energy conversion using Ag/AgCl electrodes, it is necessary to separate the electrode-related potential contribution from the membrane-derived diffusion potential. When two identical Ag/AgCl electrodes are exposed to electrolytes of different chloride activities, a redox-potential difference arises intrinsically from the unequal chloride activities at the two electrode interfaces. This condition can be realized in our salinity-gradient configuration with or without a charge-selective membrane.

Let the chloride activity be $a_{Cl^-}^{[I]}$ on reservoir I and $a_{Cl^-}^{[II]}$ on reservoir II. The Ag/AgCl half-reactions at the two electrodes can be written as:

$$\mathrm{Ag}(s) + \mathrm{Cl}^-(aq)[\mathrm{I}] \rightarrow \mathrm{AgCl}(s) + \mathrm{e}^- \tag{1}$$

$$\mathrm{AgCl}(s) + \mathrm{e}^- \rightarrow \mathrm{Ag}(s) + \mathrm{Cl}^-(aq)[\mathrm{II}] \tag{2}$$

The overall reaction is:

$$\mathrm{Cl}^-(aq)[\mathrm{I}] \rightarrow \mathrm{Cl}^-(aq)[\mathrm{II}] \tag{3}$$

Because the standard state for the identical Ag/AgCl electrodes is the same on both sides,

$$\Delta G^0 = 0; E^0 = 0 \tag{4}$$

the Nernst equation reduces to:

$$V_{\mathrm{redox}} = \frac{RT}{zF} \ln \left(\frac{a_{\mathrm{Cl}^-}^{[\mathrm{I}]}}{a_{\mathrm{Cl}^-}^{[\mathrm{II}]}} \right) \tag{5}$$

where $z = 1$ for Cl^-, R is the gas constant, T is the absolute temperature, and F is the Faraday constant.

In our measurements, the experimentally observed open-circuit voltage reflects both the membrane-derived diffusion potential and the electrode-related contribution:

$$V_{oc} = V_{\mathrm{diff}} + V_{\mathrm{redox}} \tag{6}$$

Thus, the diffusion potential generated by ion-selective transport through the PE-VMT nanochannels is obtained by:

$$V_{\mathrm{diff}} = V_{\mathrm{oc}} - V_{\mathrm{redox}} \tag{7}$$

As shown in Fig. S11, the V_{redox} values calculated from Eq. (5) agree well with the experimentally measured electrode-related potentials under identical concentration ratios, validating the separation used in this work.

Note S2. Diffusion potential by the ion-selective PE-VMT channels (V_{diff})

The PE-VMT membrane contains negatively charged, asymmetric lateral nanochannels that preferentially transport cations (primarily Na^+) from the high-salinity side to the low-salinity side. This permselective ion transport generates a diffusion potential V_{diff}, which reflects the imbalance between the diffusive fluxes of cations and anions inside the nanofluidic channels. The diffusion potential can be expressed as:

$$V_{\mathrm{diff}} = (t_+ - t_-)\frac{RT}{F}\ln\left(\frac{a_{\mathrm{high}}}{a_{\mathrm{low}}}\right) \tag{8}$$

where t_+ and t_- are the cation and anion transference numbers within the PE-VMT channels, and a_{high} and a_{low} are the activities of NaCl on the high- and low-salinity sides, respectively. The term $(t_+ - t_-)$ represents the ion selectivity (α) of the membrane.

In the ideal case of complete cation selectivity ($t_+ = 1$, $t_- = 0$), the theoretical diffusion potential is:

$$V_{\mathrm{theo}} = \frac{RT}{F}\ln\left(\frac{a_{\mathrm{high}}}{a_{\mathrm{low}}}\right) \tag{9}$$

Note S3. Membrane ion selectivity and energy conversion efficiency

The effective ion selectivity of the PE-VMT membrane can be quantified by comparing the measured diffusion potential to the theoretical value assuming 100% selectivity:

$$\alpha = (t_+ - t_-) \times 100\% = \frac{V_{diff}}{V_{theo}} \times 100\% \quad (10)$$

The corresponding energy conversion efficiency is defined as the fraction of the Gibbs free energy of mixing of the high- and low-salinity solutions that can be converted into electrical work under idealized membrane-controlled transport. For a monovalent electrolyte operated near the maximum-power condition, classical salinity-gradient theory gives

$$\eta = \frac{(t_+ - t_-)^2}{2} \times 100\% \quad (11)$$

Note S4. Power density

The output power density was calculated from the measured current–voltage characteristics after separating the membrane-derived contribution from the electrode redox contribution. The maximum output power is obtained at approximately half of the diffusion potential. Therefore, the maximum power density can be expressed as:

$$PD_{\max} = \frac{1}{4} \frac{R_{\mathrm{CH}} I_{\mathrm{diff}}^2}{A_{\mathrm{eff}}} \quad (12)$$

where R_{CH} and A_{eff} is the channel resistance and effective membrane area, respectively.

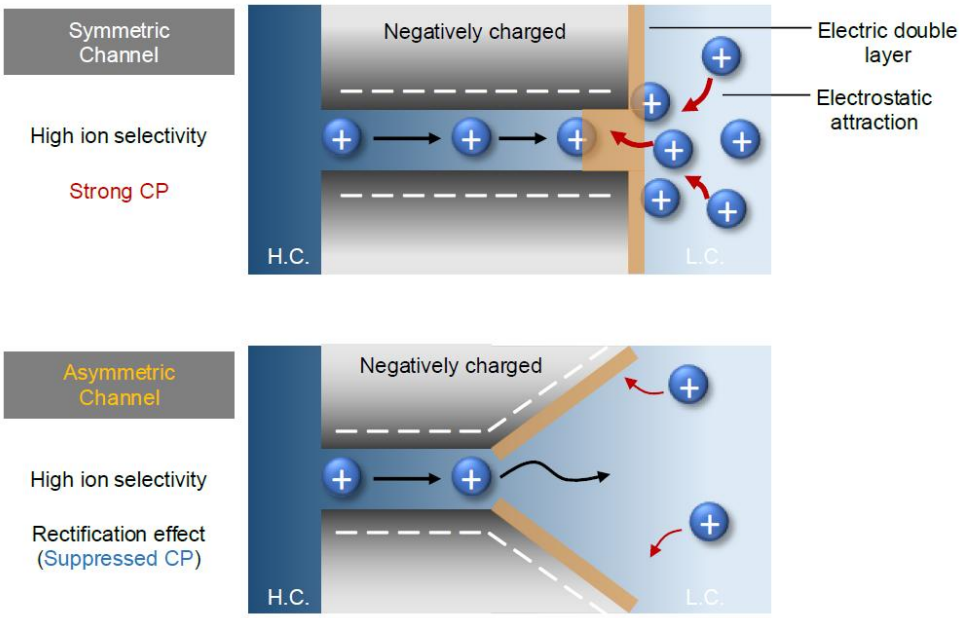

Figure S1. Influences of the channel symmetry on the ion selectivity and concentration polarization (CP). Top: In a symmetric nanochannel, the negatively charged walls induce strong electrostatic attraction, leading to significant ion accumulation at the interface and resulting in strong CP. This effect reduces the ion transport efficiency, despite the high ion selectivity. Bottom: In an asymmetric nanochannel, the geometric asymmetry modifies the ion transport behavior, suppressing CP via a rectification effect. This results in an improved ion transport efficiency while maintaining a high ion selectivity. H.C.: High-concentration region, L.C.: Low-concentration region.

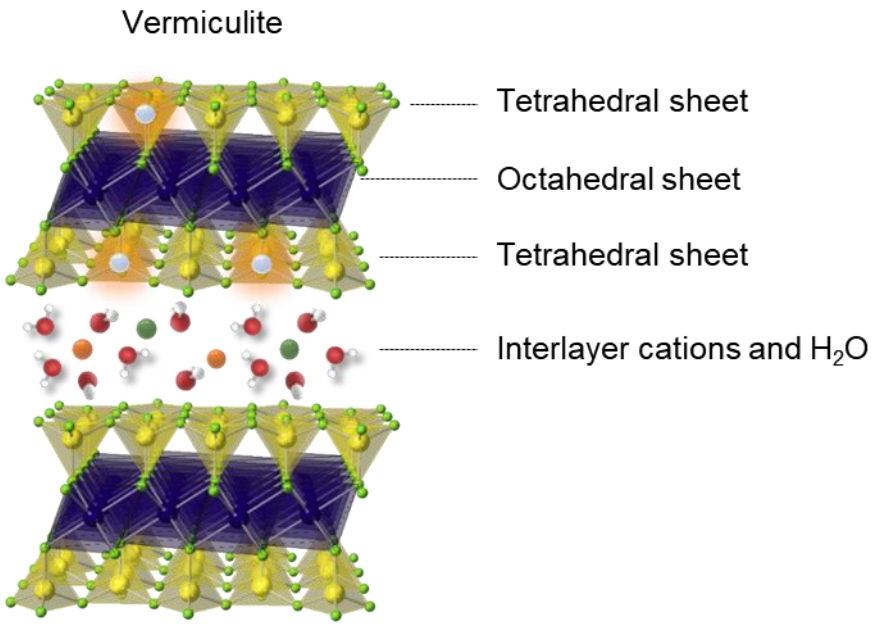

Figure S2. Schematic of the layered crystal structure of vermiculite (VMT), comprising tetra- and octahedral sheets. The interlayer region contains exchangeable cations (e.g., Mg^{2+} and K^{+}) and H_2O.

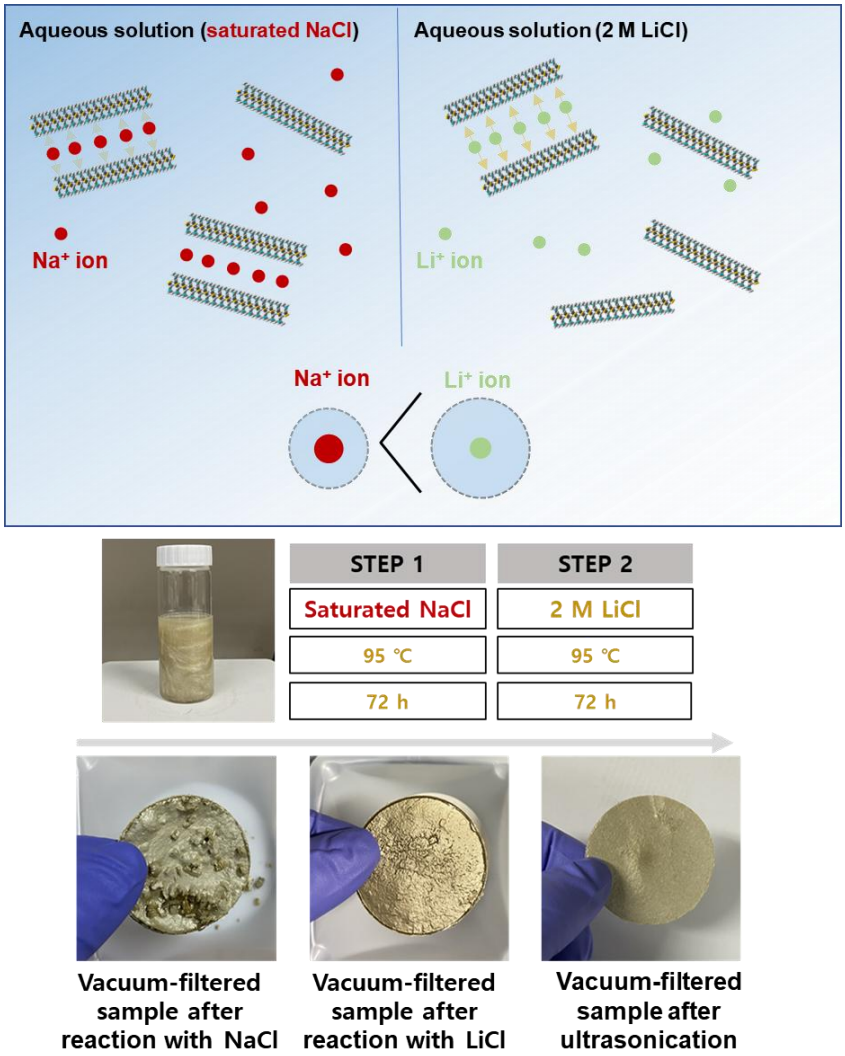

Figure S3. Two-step cation exchange for Li^+ intercalation within VMT. Top: Schematic of cation exchange in aqueous solutions. Initially, VMT is exposed to a saturated NaCl solution, where the Na^+ ions interact with the interlayer cations. In the second step, the material is treated with a 2 M LiCl solution, facilitating the exchange of Na^+ with Li^+. Bottom: Images of vacuum-filtered samples after conducting each processing step for 72 h, revealing the morphological changes. The final ultrasonication step results in a well-dispersed, homogeneous sample.

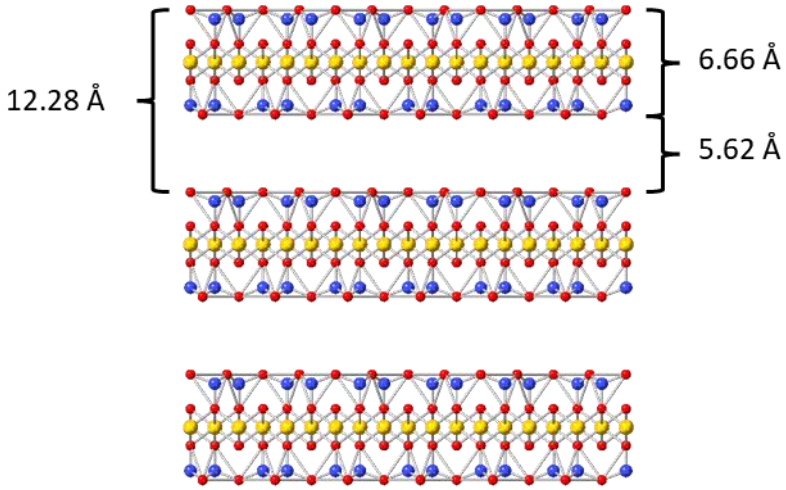

Figure S4. Crystal structure of VMT, comprising tetra- and octahedral sheets. The interlayer spacing is approximately 5.62 Å.

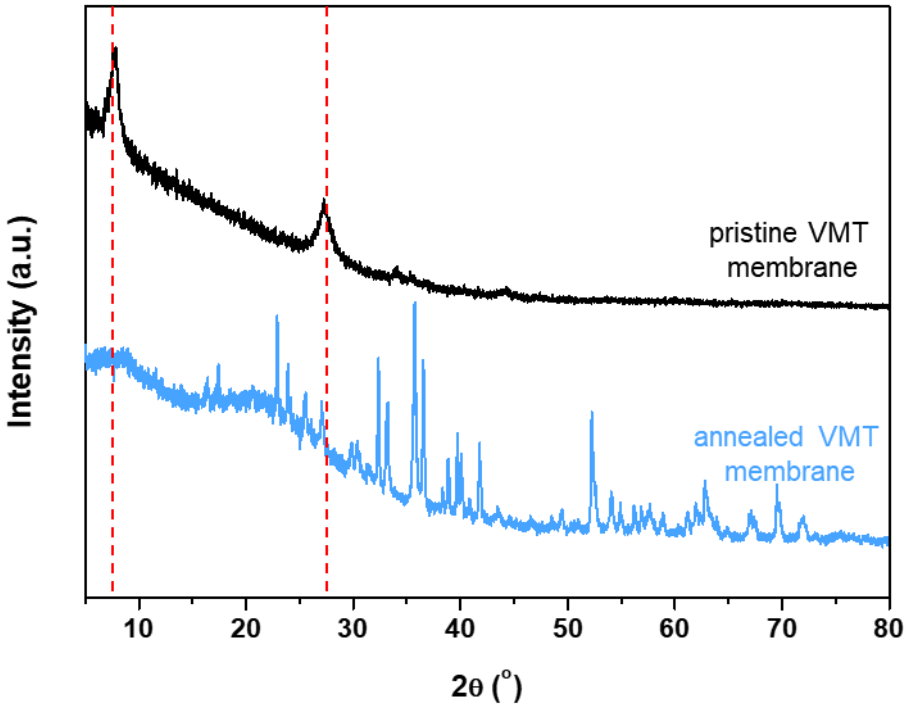

Figure S5. X-ray diffraction patterns of the pristine and annealed VMT membranes.

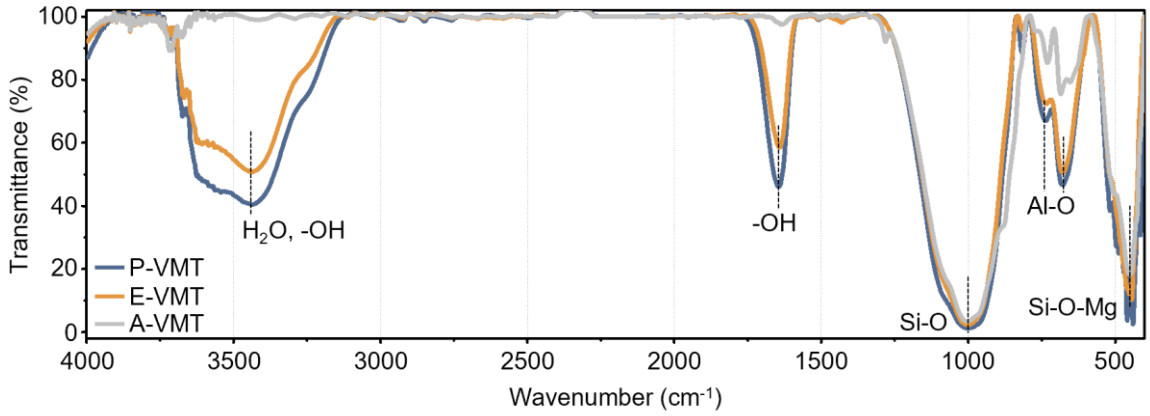

Figure S6. FT-IR spectra of P-VMT, E-VMT, and A-VMT, displaying the characteristic vibrational modes.

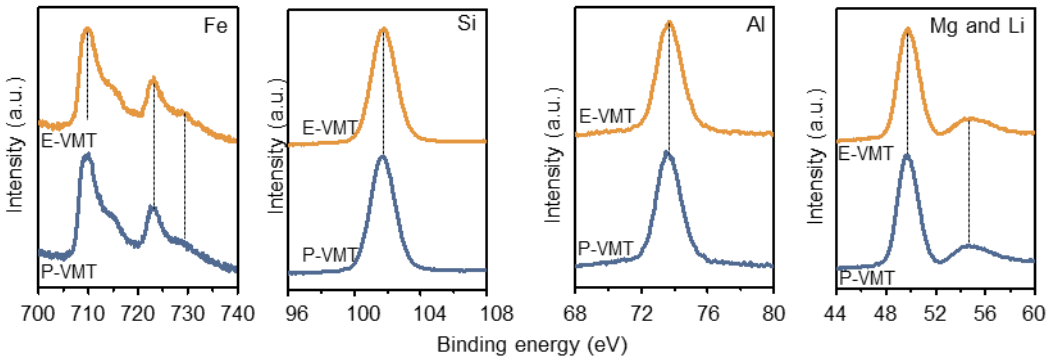

Figure S7. XPS spectra indicating the elemental compositions: Fe; Si; Al; and Mg and Li.

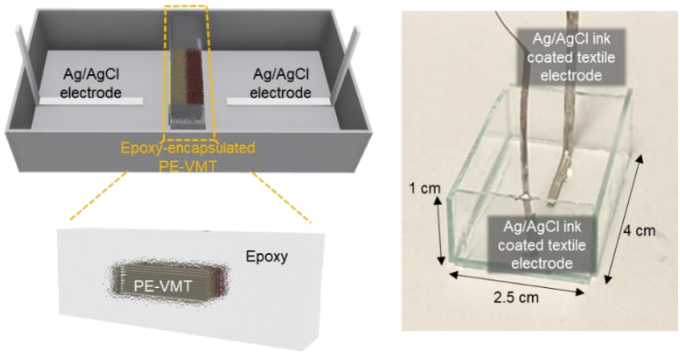

Figure S8. Schematic and image of experimental setup for measuring performance of PE-VMT.

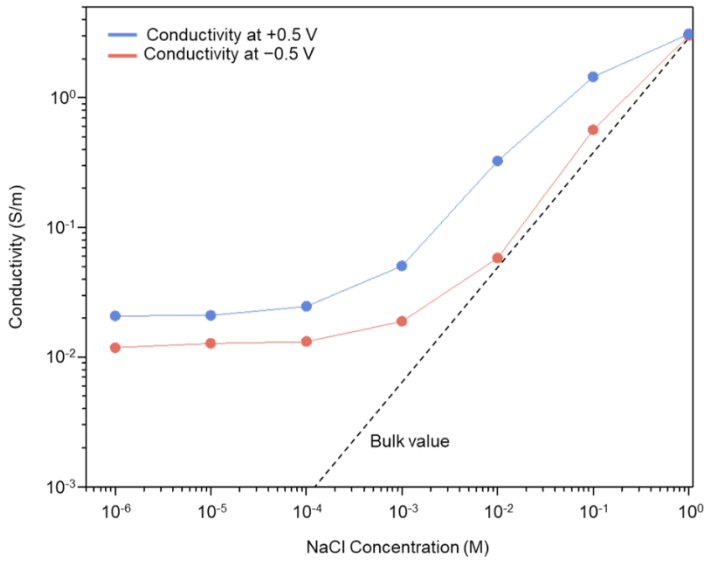

Figure S9. Ionic conductivity of the PE-VMT membrane in the intramembrane direction as a function of NaCl concentration. We recorded *I*–*V* curves from −0.5 to +0.5 V under symmetric salinity conditions and obtained the apparent conductivities at +0.5 V and −0.5 V from the linear slopes around these biases. The two curves therefore represent the conductivities in the forward and reverse directions, respectively. The dashed line shows the bulk NaCl conductivity. The values are different in the forward and backward directions at the same concentration due to the asymmetric nanochannel structure of PE-VMT.

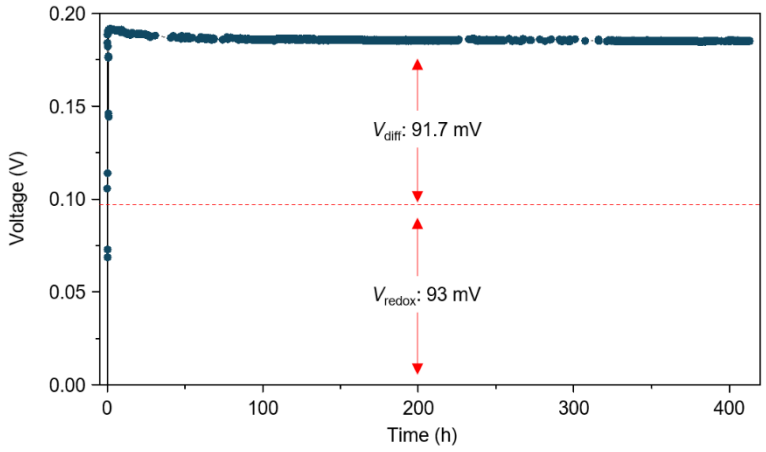

Figure S10. Open-circuit voltage (V_{oc}) as a function of time under a concentration gradient of 50 (0.5 M/0.01 M NaCl)

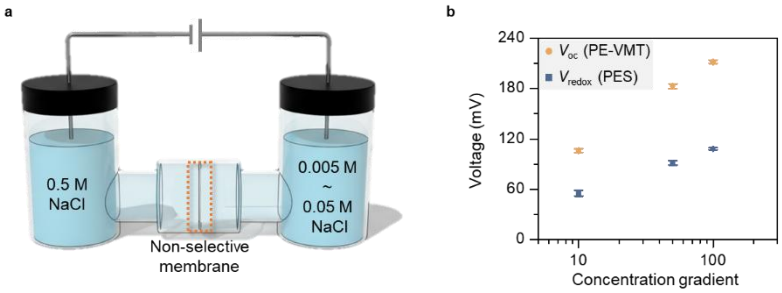

Figure S11. Ag/AgCl electrode configuration used to quantify the redox potential V_{redox} in the absence of an ion-selective membrane. (a) The two reservoirs contain 0.5 M NaCl (left) and 0.005–0.05 M NaCl (right), separated only by a nonselective membrane (Polyethersulfone (PES) membrane of pore size 400 nm) so that no additional diffusion potential is generated across the junction. Identical Ag/AgCl electrodes are immersed in each reservoir. (b) Measured data of V_{redox} (non-selective membrane) and V_{oc} (V_{redox} + V_{diff}, PE-VMT membrane) under various concentration gradients. Error bars denote standard deviation.

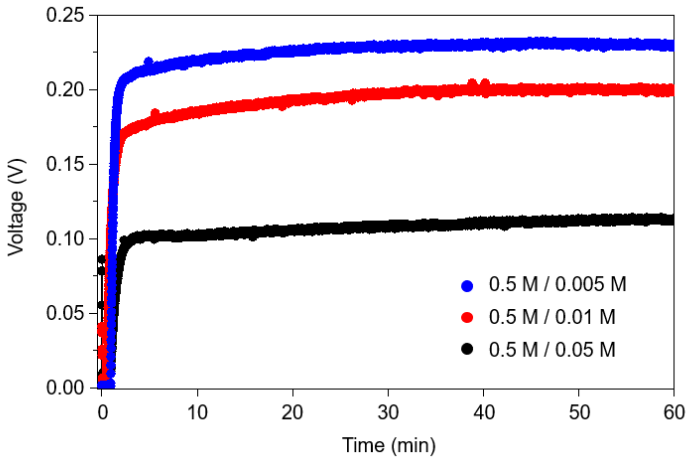

Figure S12. Voltage output of PE-VMT membranes as a function of time under concentration gradients of 10, 50, and 100. The steady-state voltages are nearly twice the Ag/AgCl redox potentials measured in the nonselective configuration (Fig. S11), indicating that the additional contribution arises from the membrane-derived diffusion potential and that the ion selectivity is maintained under these salinity gradients.

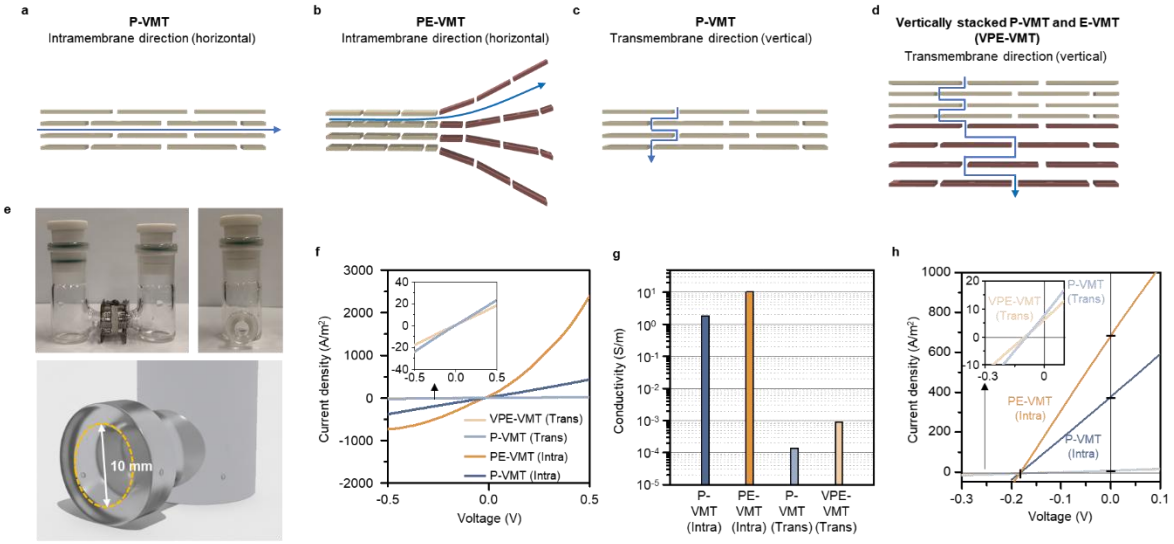

Figure S13. Comparison of ion transport and salinity-gradient energy conversion performance of vermiculite-based membranes in the intramembrane (horizontal) and transmembrane (vertical) directions. (a) Schematic of intramembrane (horizontal) ion transport through pristine P-VMT. (b) Schematic of intramembrane (horizontal) ion transport through PE-VMT. (c) Schematic of transmembrane (vertical) ion transport through P-VMT. (d) Schematic of the transmembrane (vertical) configuration used as a reference for PE-VMT, where a pristine VMT layer and an expanded VMT layer are vertically stacked to form VPE-VMT (vertically stacked P-VMT and E-VMT). All transmembrane measurements were conducted using an H-cell configuration. (e) Photographs of the H-cell used for transmembrane measurements and the effective aperture (10 mm diameter) used for area normalization. (f) Current density–voltage characteristics measured under symmetric salinity conditions for P-VMT (intra), PE-VMT (intra), P-VMT (trans), and VPE-VMT (trans). (g) Ionic conductivity extracted from the slope of the *I–V* curves near 0 V (−0.05 to +0.05 V) under symmetric salinity, highlighting the much higher conductivity in the intramembrane direction compared to the transmembrane direction. (h) *I–V* characteristics of membranes under a 50-fold salinity gradient.

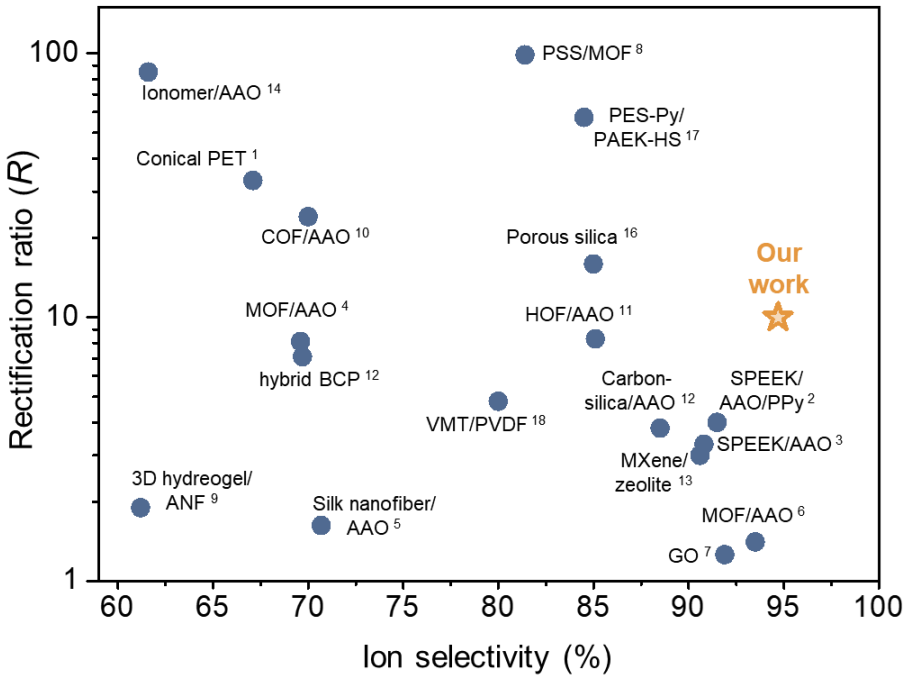

Figure S14. Rectification ratios and ion selectivities of the partially expanded VMT (PE-VMT) membrane and various bipolar nanofluidic energy-harvesting systems.

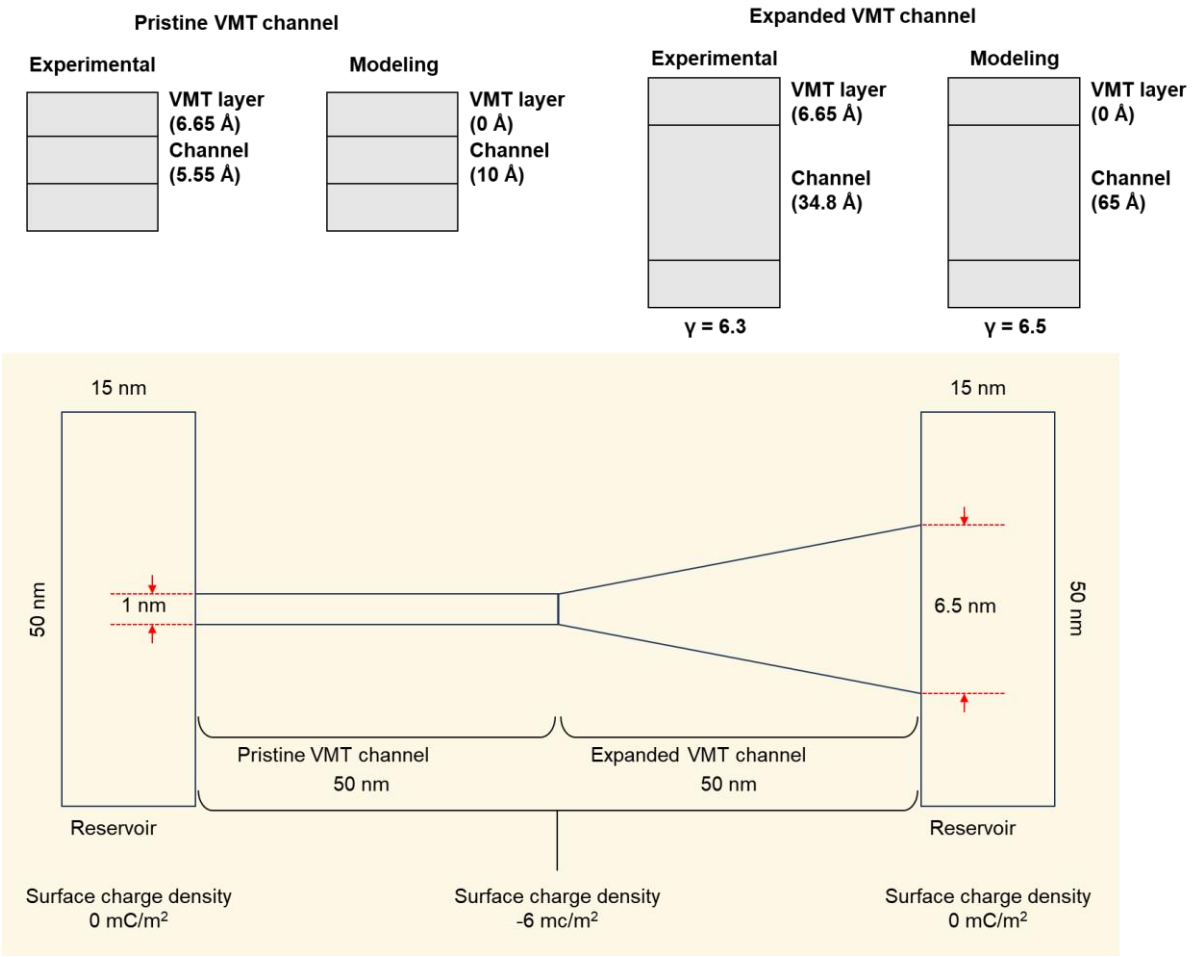

Figure S15. Numerical simulation setup for PE-VMT.

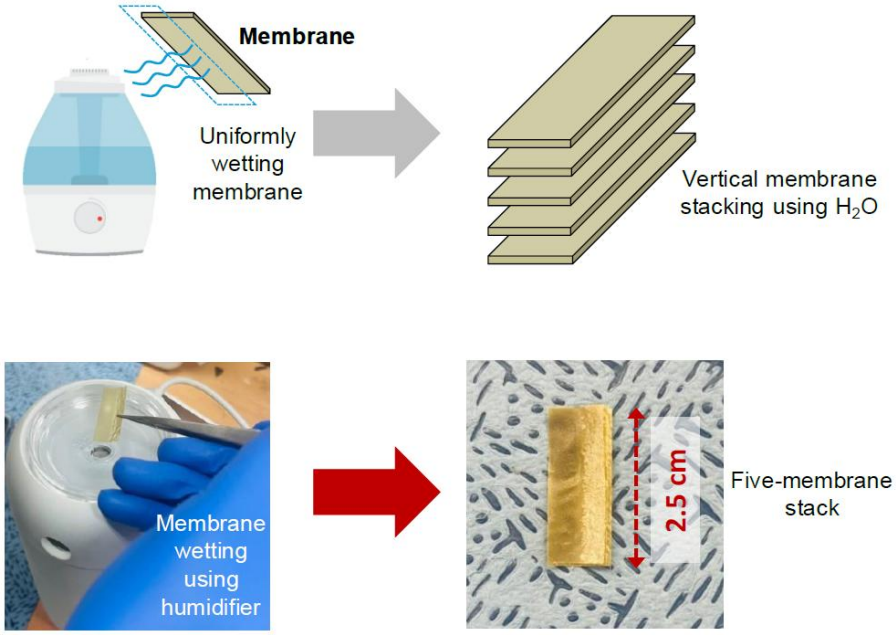

Figure S16. Fabrication of the stacked PE-VMT membranes (device) using the self-healing property of VMT.

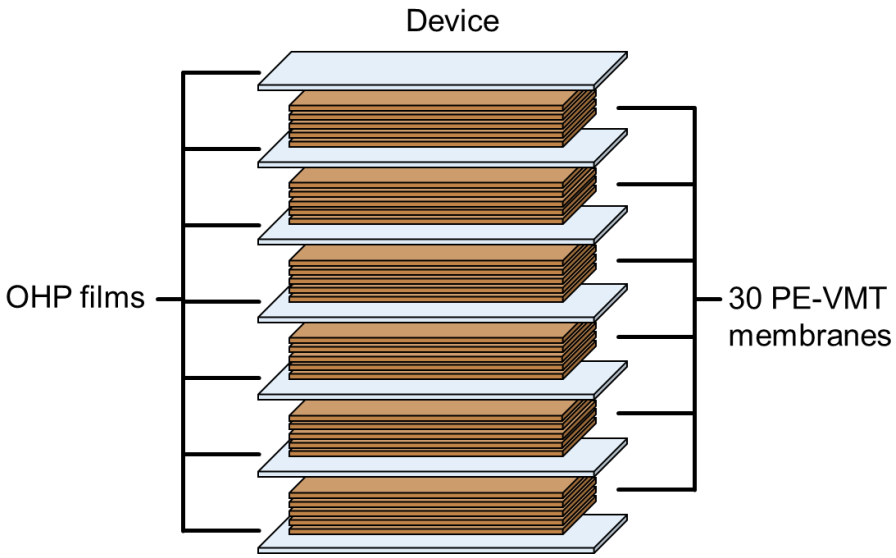

Figure S17. Schematic of a stacked PE-VMT membrane device. The device comprises multiple layers of PE-VMT membranes, with 30 membranes per stack, separated by overhead projector (OHP) films for structural support. This modular stacking approach enhances the ion transport efficiency and mechanical stability, enabling scalable energy-harvesting applications.

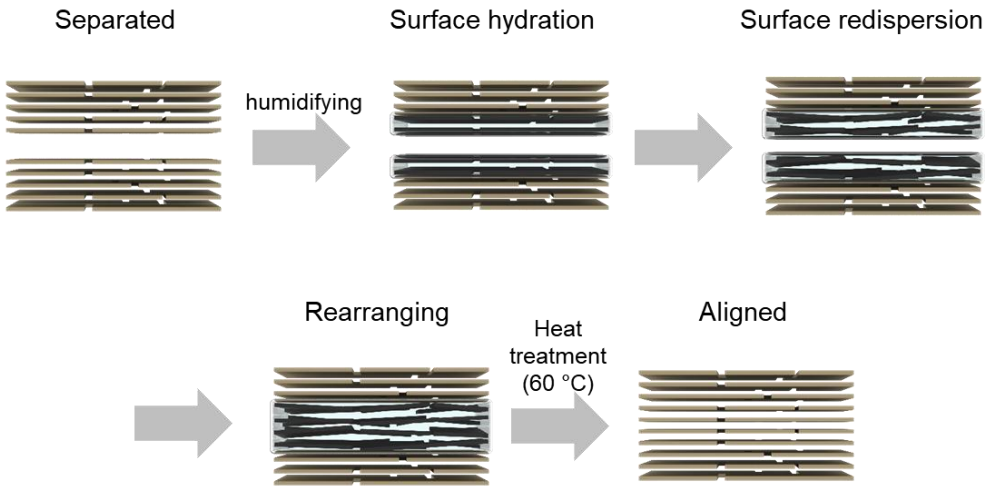

Figure S18. Schematic of the self-assembly of VMT. Initially, separate VMT layers undergo surface hydration upon exposure to humidity, leading to surface redispersion. The hydrated nanosheets subsequently rearrange, forming a more compact structure. Controlled heating at 60 °C further enhances the alignment, resulting in a well-ordered layered VMT structure. This process demonstrates a scalable approach for use in fabricating highly structured VMT membranes.

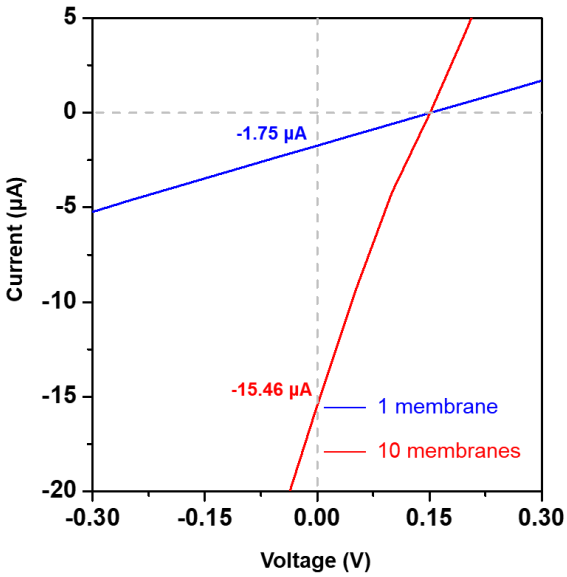

Figure S19. Current-potential (*I–V*) characteristics of the single and self-healing 10-layer stacked membranes. *I–V* curves measured under a concentration gradient of 50 across the channel. The single membrane (blue curve) exhibits a smaller short-circuit current (1.75 μA), whereas the 10-layer stacked membrane (red curve) displays a significantly larger short-circuit current (15.46 μA), indicating its enhanced ion transport due to the improved interfacial connectivity and self-healing effects of the stacked configuration.

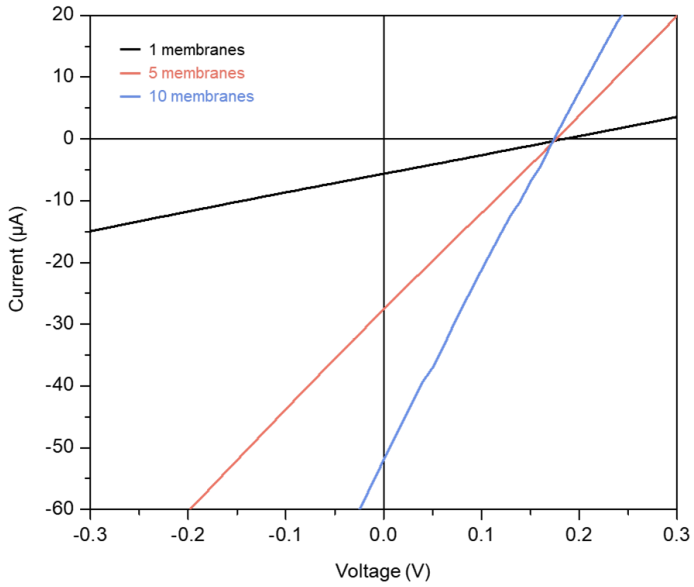

Figure S20. Current–potential (*I–V*) characteristics of stacked PE-VMT cells (w = 25 mm, L = 8 mm). *I–V* curves were recorded under a concentration gradient of 50 across the channel. The short-circuit current increases nearly linearly with the number of stacked elements, while the open-circuit voltage remains essentially unchanged, confirming that the stacking-dependent scaling observed in Fig. S19 is preserved when using the larger membrane.

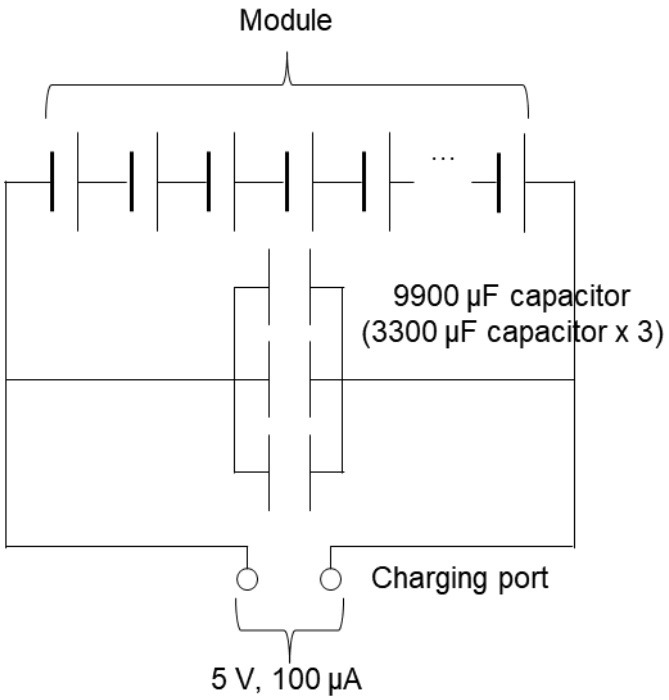

Figure S21. Schematic of a PE-VMT module connected to a capacitor. The PE-VMT module comprises 30 devices connected in series, enabling efficient energy harvesting. The output is linked to a 9900 μF capacitor formed by three 3300 μF capacitors in parallel, serving as an energy-storage component. The system provides a stable output of 5 V and 100 μA via a designated charging port, demonstrating its capacity for use in low-power electronic applications.

Table S1. Comparison of the performances of various materials.

Material	Dimension	Power density (W/m^2)	Effective area (μm^2)	No.
vertically stacked graphene oxide (GO)	2D	10.6	3550	[19]
vermiculite	2D	4.1	30 000	[20]
oppositely charged GO	2D	0.7	2 800 000	[21]
oppositely charged GO	2D	0.7	42 000	[21]
MXene/Kevlar nanofiber	2D	3.7	30 000	[22]
MXene/BN	2D	2.3	30 000	[23]
MXene	2D	4.6	200 000	[24]
MXene	2D	12.8	25 000	[25]
MoS_2/cellulose nanofiber	2D	5.2	30 000	[26]
GO/silk nanofiber	2D	5.07	30 000	[27]
GO/cellulose nanofiber	2D	4.19	30 000	[28]
BN/aramid nanofiber	2D	0.6	3 140 000	[29]
BN/aramid nanofiber	2D	5.9	30 000	[29]
MXene/cellulose	2D/3D	0.91	1 000 000	[30]
GO/CA membrane	2D/3D	0.13	200 000	[31]
Tempo-oxidized cellulose nanofiber	3D	0.96	9 000 000	[32]
SPEEK/AAO	3D	4.8	300 000 000	[3]
Silk nanofiber/AAO	3D	2.86	30 000	[33]
bacterial cellulose biofilm	3D	0.23	1 800 000	[34]
Our work	2D	7.95	7640	
Our work	2D	6.05	229 200	
Our work	2D	5.93	6 876 000	

Table S2. Comparison of vermiculite-based membranes for salinity gradient energy conversion at 50-fold salinity gradient

Material	Ion selectivity (%)	Energy conversion efficiency (%)	Power density (W/m^2)	Effective area (μm^2)	No.
Lamellar porous vermiculite membrane	64	20.5	4.1	30,000	[20]
Biomimetic 2D vermiculite membrane	-	-	0.07 – 0.08	-	[35]
Carbonized 2D vermiculite-based composite membrane	74	27.4	-	10^{10}	[36]
Na-vermiculite Å-scale capillary	83	34.4	0.05 – 9.6	528	[37]
Vermiculite/PVDF	60	18	5.45	-	[38]
Our work (cell)	94.9	45.0	7.95	7,640	
Our work (device)	92.5	42.7	6.05	229,200	
Our work (module)	86.0	37.0	5.93	6,876,000	

References

1. Laucirica, G. *et al.* Shape matters: Enhanced osmotic energy harvesting in bullet-shaped nanochannels. *Nano Energy* **71**, 104612 (2020).
2. Hao, J. *et al.* A Euryhaline-Fish-Inspired Salinity Self-Adaptive Nanofluidic Diode Leads to High-Performance Blue Energy Harvesters. *Adv. Mater.* **34**, 2203109 (2022).
3. Hou, S. *et al.* Charged porous asymmetric membrane for enhancing salinity gradient energy conversion. *Nano Energy* **79**, 105509 (2021).
4. Yao, C. *et al.* Enhancing osmotic energy conversion with functionalized UiO-66-NH2-based heterogeneous membrane. *J. Membr. Sci.* **707**, 122999 (2024).
5. Xin, W. *et al.* High-performance silk-based hybrid membranes employed for osmotic energy conversion. *Nat. Commun.* **10**, 3876 (2019).
6. Liu, Y.-C., Yeh, L.-H., Zheng, M.-J. & Wu, K. C.-W. Highly selective and high-performance osmotic power generators in subnanochannel membranes enabled by metal-organic frameworks. *Sci. Adv.* **7**, eabe9924 (2021).
7. Bang, K. R., Kwon, C., Lee, H., Kim, S. & Cho, E. S. Horizontally Asymmetric Nanochannels of Graphene Oxide Membranes for Efficient Osmotic Energy Harvesting. *ACS Nano* **17**, 10000–10009 (2023).
8. Li, R., Jiang, J., Liu, Q., Xie, Z. & Zhai, J. Hybrid nanochannel membrane based on polymer/MOF for high-performance salinity gradient power generation. *Nano Energy* **53**, 643–649 (2018).
9. Zhang, Z. *et al.* Improved osmotic energy conversion in heterogeneous membrane boosted by three-dimensional hydrogel interface. *Nat. Commun.* **11**, 875 (2020).
10. Chen, M. *et al.* In Situ Growth of Imine-Bridged Anion-Selective COF/AAO Membrane for Ion Current Rectification and Nanofluidic Osmotic Energy Conversion. *Adv. Funct. Mater.* **33**, 2302427 (2023).
11. Wang, H. *et al.* In Situ Synthesized HOF Ion Rectification Membrane with Ultrahigh Permselectivity for Nanofluidic Osmotic Energy Harvesting. *Adv. Funct. Mater.* **35**, 2412477 (2025).
12. Zhou, S. *et al.* Interfacial Super-Assembly of Ordered Mesoporous Carbon-Silica/AAO

Hybrid Membrane with Enhanced Permselectivity for Temperature- and pH-Sensitive Smart Ion Transport. *Angew. Chem. Int. Ed.* **60**, 26167–26176 (2021).

13. Zhou, J. *et al.* Maximizing Ion Permselectivity in MXene/MOF Nanofluidic Membranes for High-Efficient Blue Energy Generation. *Adv. Funct. Mater.* **32**, 2209767 (2022).

14. Xiao, T. *et al.* pH-Resistant Nanofluidic Diode Membrane for High-Performance Conversion of Salinity Gradient into Electric Energy. *Energy Technol.* **7**, 1800952 (2019).

15. Zhang, Z. *et al.* Ultrathin and Ion-Selective Janus Membranes for High-Performance Osmotic Energy Conversion. *J. Am. Chem. Soc.* **139**, 8905–8914 (2017).

16. Yang, Y. *et al.* Unipolar Ionic Diode Nanofluidic Membranes Enabled by Stepped Mesochannels for Enhanced Salinity Gradient Energy Harvesting. *J. Am. Chem. Soc.* **146**, 19580–19589 (2024).

17. Zhu, X. *et al.* Unique ion rectification in hypersaline environment: A high-performance and sustainable power generator system. *Sci. Adv.* **4**, eaau1665 (2018).

18. Wang, J. *et al.* Unlocking osmotic energy harvesting potential in challenging real-world hypersaline environments through vermiculite-based hetero-nanochannels. *Nat. Commun.* **15**, 608 (2024).

19. Zhang, Z. *et al.* Vertically Transported Graphene Oxide for High-Performance Osmotic Energy Conversion. *Adv. Sci.* **7**, 2000286 (2020).

20. Cao, L. *et al.* Lamellar porous vermiculite membranes for boosting nanofluidic osmotic energy conversion. *J. Mater. Chem. A* **9**, 14576–14581 (2021).

21. Sheng, N. *et al.* Enhanced salinity gradient energy harvesting with oppositely charged bacterial cellulose-based composite membranes. *Nano Energy* **101**, 107548 (2022).

22. Zhang, Z. *et al.* Mechanically strong MXene/Kevlar nanofiber composite membranes as high-performance nanofluidic osmotic power generators. *Nat. Commun.* **10**, 2920 (2019).

23. Yang, G. *et al.* Stable $Ti_3C_2T_x$ MXene–Boron Nitride Membranes with Low Internal Resistance for Enhanced Salinity Gradient Energy Harvesting. *ACS Nano* **15**, 6594–6603 (2021).

24. Ding, L. *et al.* Oppositely Charged $Ti_3C_2T_x$ MXene Membranes with 2D Nanofluidic

Channels for Osmotic Energy Harvesting. *Angew. Chem.* **132**, 8798–8804 (2020).

25. Hong, S. *et al.* Porous $Ti_3C_2T_x$ MXene Membranes for Highly Efficient Salinity Gradient Energy Harvesting. *ACS Nano* **16**, 792–800 (2022).

26. Zhu, C. *et al.* Metallic Two-Dimensional MoS_2 Composites as High-Performance Osmotic Energy Conversion Membranes. *J. Am. Chem. Soc.* **143**, 1932–1940 (2021).

27. Xin, W. *et al.* Biomimetic Nacre-Like Silk-Crosslinked Membranes for Osmotic Energy Harvesting. *ACS Nano* **14**, 9701–9710 (2020).

28. Wu, Y. *et al.* Enhanced ion transport by graphene oxide/cellulose nanofibers assembled membranes for high-performance osmotic energy harvesting. *Mater. Horiz.* **7**, 2702–2709 (2020).

29. Chen, C. *et al.* Bio-inspired Nanocomposite Membranes for Osmotic Energy Harvesting. *Joule* **4**, 247–261 (2020).

30. Xu, Y. *et al.* Two-dimensional lamellar MXene/three-dimensional network bacterial nanocellulose nanofiber composite Janus membranes as nanofluidic osmotic power generators. *Electrochimica Acta* **412**, 140162 (2022).

31. Jia, P. *et al.* The Combination of 2D Layered Graphene Oxide and 3D Porous Cellulose Heterogeneous Membranes for Nanofluidic Osmotic Power Generation. *Molecules* **26**, 5343 (2021).

32. Xu, Y., Song, Y. & Xu, F. TEMPO oxidized cellulose nanofibers-based heterogenous membrane employed for concentration-gradient-driven energy harvesting. *Nano Energy* **79**, 105468 (2021).

33. Gao, J. *et al.* High-Performance Ionic Diode Membrane for Salinity Gradient Power Generation. *J. Am. Chem. Soc.* **136**, 12265–12272 (2014).

34. Wu, Z. *et al.* Oppositely charged aligned bacterial cellulose biofilm with nanofluidic channels for osmotic energy harvesting. *Nano Energy* **80**, 105554 (2021).

35. Liu, Y. *et al*. Biomimetic two-dimensional vermiculite nanofluidic membranes for stable salinity-gradient energy conversion. *Inorg. Chemistry* **62**, 5400-5407 (2025).

36. Yang, L. *et al.* Large-area freestanding carbonized 2D vermiculite-based composite membranes for osmotic energy harvesting. *Chem. Eng. J.* **508**, 160922 (2025).

37. Aparna, R. *et al.* Ion-hydration-controlled large osmotic power with arrays of angstrom scale capillaries of vermiculite. *Cell Rep. Phys. Sci.* **4**, 101717 (2023).

38. Wang, J. *et al.* Unlocking osmotic energy harvesting potential in challenging real-world hypersaline environments through vermiculite-based hetero-nanochannels. *Nat. Commun.* **15**, 608 (2024).